

High-fidelity non-adiabatic dark state gates for neutral atoms

Nader Mostaan  ^{1,*} Kapil Goswami  ¹ Peter Schmelcher  ^{1,2} and Rick Mukherjee  ^{1,3,4}

¹ Zentrum für Optische Quantentechnologien, Universität Hamburg,
Luruper Chaussee 149, 22761 Hamburg, Germany

² The Hamburg Centre for Ultrafast Imaging, Universität Hamburg,
Luruper Chaussee 149, 22761 Hamburg, Germany

³ Department of Physics & Astronomy, University of Tennessee, Chattanooga, TN 37403, USA

⁴ UTC Quantum Center, University of Tennessee, Chattanooga, TN 37403, USA

(Dated: February 17, 2026)

Rydberg blockade gates are the most experimentally mature entangling operations in neutral-atom quantum processors, combining fast gate times with simple control, but their performance degrades at larger interatomic separations and remains sensitive to motional and technical noise. Non-blockade gate schemes, such as dark-state and geometric protocols, offer complementary robustness but typically rely on complex and experimentally demanding control. Here we show that quantum optimal control enables non-blockade gate schemes to be implemented using the experimentally established pulse-shaping techniques developed for blockade-based gates. Focusing on the dark-state gate, we construct non-adiabatic implementations that preserve the intrinsic robustness of adiabatic dark-state protocols while achieving gate times comparable to time-optimal blockade gates using only smooth, experimentally feasible pulses. The resulting gates exhibit enhanced resilience to motional coupling, laser noise, and interaction inhomogeneity, particularly near and beyond the blockade radius. This work establishes a practical route to fast, robust two-qubit gates without increased experimental complexity.

I. INTRODUCTION

Gate-based quantum computation has emerged as a leading paradigm in quantum science and technology, offering significant potential for applications such as the simulation of complex quantum materials [1–4], solving classically intractable optimization problems [5–9], and design of novel molecules and pharmaceuticals [10–12].

The ability to perform quantum information processing tasks in gate-based quantum devices requires the precise control of individual qubits and implementation of high-fidelity entangling operations [13–15]. Such control enables quantum algorithms [16], error correction [17, 18], and the generation of complex entangled states [19], which are essential for realizing practical quantum technologies. In recent years, significant progress has been made across several physical platforms, including superconducting circuits [20], trapped ions [21], photonic systems [22], and neutral atoms [23, 24], each offering complementary advantages for scalability and coherence [25]. In all these platforms, the fidelity of entangling gates directly impacts the performance of algorithms and the feasibility of fault-tolerant architectures, motivating extensive research into optimizing gate protocols across different qubit platforms [21, 26–28].

Significant efforts have been devoted to designing high-fidelity multi-qubit and two-qubit gates in a variety of physical systems. In superconducting circuits, controlled-NOT (CNOT) and CZ gates have been realized with fidelities exceeding 0.99 using microwave-driven

interactions [29–32]. Photonic systems have demonstrated probabilistic entangling gates through linear optics and measurement-induced interactions [33, 34].

In neutral atom platforms, two-qubit gates have been implemented using strong interactions between highly excited Rydberg states [35–37]. Neutral atom systems offer unique advantages for scalable quantum computation, due to various factors, among them long coherence times [35], flexible and reconfigurable arrays in different dimensions [38–40] and long-range, controllable interactions via Rydberg states, to name a few. Individual atoms can be trapped in optical tweezers with high spatial resolution and rearranged into arbitrary geometries [41], while Rydberg excitations provide strong, controllable interactions that enable fast entangling gates while maintaining long coherence times [35, 36].

Implementing high-fidelity two-qubit gates in neutral atom systems is particularly significant, as they are the fundamental building blocks for multi-qubit operations and scalable quantum algorithms. The main goals are to achieve fast gate operations, minimize residual entanglement with motional degrees of freedom, and maintain robustness against technical noise. Both controlled-Z (CZ) and controlled-NOT (CNOT) gates have been demonstrated experimentally using Rydberg interactions, with fidelities currently approaching the 0.97–0.99 range [36, 37]. While the progress in implementing gates with this fidelities has been impressive, in order to be able to realize many standard error correcting codes, the infidelities have to reach below 10^{-4} [42].

One of the most widely used and experimentally mature implementations of entangling gates in neutral-atom platforms is based on the Rydberg blockade mechanism, which we refer to here as *blockade gates* [35, 45–

* nader.mostaan@uni-hamburg.de

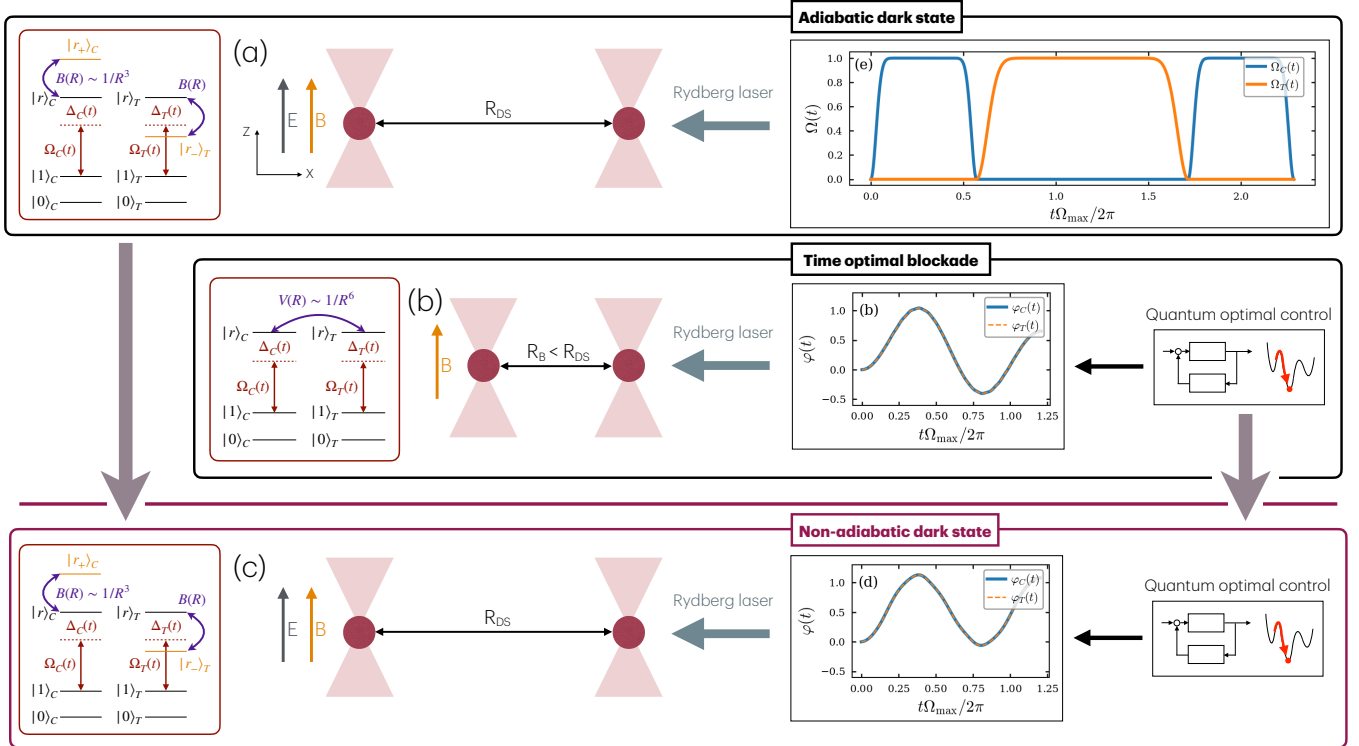


FIG. 1. Concepts of blockade, adiabatic and non-adiabatic dark state gates. (a) Schematic of the adiabatic dark state gate: to realize a dark state gate, a constant electric field is applied along the quantization axis to Stark-tune a Förster resonance. A $\pi - 2\pi - \pi$ sequence is applied to the qubits to realize the gate [43]. The level diagram including the dipole-dipole coupling of Rydberg states as well as the Rabi couplings is shown in the inset. (b) Schematic of the time optimal blockade gate: the blockade gate entirely relies on the van der Waals interaction, and only a magnetic field is applied. Due to the $1/R^6$ dependence of the van der Waals interaction, the interatomic distance must fall below the blockade radius, putting more stringent constraint on the interatomic distance compared to the dark state gates. On the other hand, the interatomic distance for implementing the dark state gate does not suffer from this restriction (demonstrated in the figure by having $R_B < R_{DS}$). The Rabi pulses are shaped by the application of quantum optimal control (QOC) to find time optimal pulses. The optimal pulses are global [44] with the Rabi coupling equal to the maximum allowed value, whereas the phases for the control and target qubits $\varphi_C(t)$ and $\varphi_T(t)$ are shown in the inset. (c) By combining the level scheme of dark state gates with QOC pulse shaping, a *non-adiabatic dark state* gate is achieved. Similar to the blockade gate, the time optimal non-adiabatic dark state gate exhibits global pulses, with the Rabi frequencies set to their maximal value, and equal control and target pulse phases. This non-adiabatic gate design benefits from the advantages of both the adiabatic dark state gate and the time optimal blockade gate. The level scheme along with the detailed implementation of the CZ gate for each approach is explained in the text.

47]. These gates exploit strong van der Waals interactions between Rydberg states to implement conditional logic operations such as controlled-phase and controlled-Z gates [35, 47]. Blockade gates offer several key advantages: gate times reduced by the application of quantum optimal control techniques [44, 48], simple pulse sequences, and natural compatibility with large-scale neutral-atom arrays [35, 47]. A standard blockade gate can be implemented using only a small number of laser pulses and does not require cyclic evolution, auxiliary microwave fields [49], or highly structured optimal-control waveforms. Despite these advantages, blockade-based gates suffer from intrinsic limitations. The dominant error sources include spontaneous emission from Rydberg states, laser phase and intensity noise, imperfect blockade due to finite interaction strengths, atomic motion, and spatial inhomogeneity, all of which lead to leakage

and phase errors, as analyzed in detail in many previous works [47, 49–51]. These challenges have motivated extensive efforts to improve blockade gate performance using pulse shaping [36, 52], quantum optimal control [44, 53], adiabatic or echo-based protocols [26, 54], and hybrid schemes incorporating geometric phases or error-suppressing techniques [55]. While blockade gates currently represent the leading neutral-atom entangling-gate technology, substantial room remains for improvement on the path toward fault-tolerant operation.

On the other hand, *non-blockade* gate schemes offer complementary advantages to blockade-based approaches by relaxing the requirement of strong interaction-induced level shifts. In particular, dark state [43, 56] and interference-based gates suppress population of the $|rr\rangle$ state, reducing sensitivity to atomic motion, imperfect blockade, and spatial inhomogeneity [43, 57]. Geomet-

ric and holonomic gates exploit geometric phase accumulation, providing intrinsic robustness against certain control errors such as pulse-area and timing imperfections [58, 59]. Together, these approaches provide flexible mechanisms to mitigate specific error sources.

However, these advantages typically come at the cost of increased experimental complexity. Many non-blockade approaches rely on intricate multi-level coupling schemes, multi-photon excitation, cyclic parameter modulation, auxiliary microwave control, or finely shaped and tightly synchronized laser pulses with strict phase and amplitude requirements. Examples include holonomic and geometric gates that depend on cyclic evolution in multi-level Rydberg manifolds [58], non-adiabatic dark-path geometric gates requiring off-resonant multilevel driving [57], and microwave-assisted resonant dipole-dipole gates that combine optical and microwave fields for entanglement generation [49, 60]. Additionally, schemes based on Rydberg antiblockade with adiabatic passage demand finely tuned detunings and pulse sequences [60]. While these approaches offer additional flexibility or robustness against specific error sources, they typically come at the cost of increased experimental overhead.

In this context, an especially promising direction is to investigate whether key elements of non-blockade gate schemes can be incorporated into experimentally established blockade-based architectures with minimal modification. Achieving the robustness benefits of non-blockade protocols while retaining the simplicity, controllability, and scalability of standard blockade-gate pulse designs would represent a significant advance for neutral-atom quantum processors.

Quantum optimal control (QOC) provides a powerful framework to pursue this goal. QOC has been successfully applied across a wide range of neutral-atom and Rydberg platforms, including the preparation of exotic many-body states [61, 62], generation of GHZ states [63], and the realization of fast two- and three-qubit gates [44]. In particular, time-optimal controlled-phase gates based on blockade interactions have demonstrated the ability of QOC to push gate performance close to fundamental limits [64]. These successes naturally motivate the question of whether optimal control can similarly be used to reformulate and improve non-blockade-based gate schemes within experimentally realistic constraints.

This leads to several key questions addressed in this work. Is it possible to realize non-adiabatic extensions of traditionally adiabatic non-blockade gates using the same pulse-shaping capabilities developed for blockade gates? What are the minimal ingredients from non-blockade schemes that must be introduced to gain their advantages, and how do these modifications compare—both conceptually and quantitatively—to established blockade-based implementations? Crucially, can such hybrid approaches achieve competitive or even superior performance relative to existing time-optimal blockade gates, while retaining experimental simplicity?

Here we demonstrate that these goals can indeed be

achieved for the dark state gate. Using quantum optimal control, we construct non-adiabatic implementations of this intrinsically adiabatic gate scheme that require only smooth, experimentally feasible control pulses. Remarkably, the resulting gates not only achieve significantly reduced operation times, but also exhibit enhanced robustness against internal-motional coupling as well as amplitude and phase noise, particularly at larger interatomic separations. In this way, the optimized dark state gate combines the speed characteristic of time-optimal blockade gates with the intrinsic resilience of dark state-based protocols.

A key insight underlying this improvement is the trade-off between non-adiabatic errors and gate duration. While faster, non-adiabatic evolution can increase the population leakage into doubly excited Rydberg states, the reduced exposure time to decoherence and technical noise can compensate for this effect. We explicitly show that, within an optimal-control framework, this balance can be favorably tuned to yield a net reduction in gate error.

Overall, our results demonstrate that non-blockade gate concepts can be meaningfully integrated into blockade-based experimental architectures without resorting to complex shortcut-to-adiabaticity techniques or substantially increasing experimental complexity. This approach enables high-fidelity, fast two-qubit gates at larger atomic separations, opening new avenues for scalable neutral-atom quantum processors that combine speed, robustness, and experimental practicality.

This work is structured as follows. Section II introduces the necessary background on the physics of the blockade and the dark state gates. Section III discussed the pulse sequences used to implement the time optimal blockade as well as the adiabatic and non-adiabatic dark state gates. In Section IV we analyze different sources of errors for the non-adiabatic dark state gate and compare its response to error sources to the adiabatic dark state and the time optimal blockade gate. Finally, we provide our conclusions and outlook in Section V.

II. TWO-QUBIT GATES WITH RYDBERG ATOMS

Two-qubit gate implementations in neutral-atom platforms rely on encoding the computational basis states $\{|0\rangle, |1\rangle\}$ in long-lived atomic ground or hyperfine states of atoms, in alkaline and alkaline earth atoms, while entangling operations are mediated through laser-induced excitation of these states to highly excited Rydberg levels. The strong and state-dependent interactions between Rydberg excitations provide the essential nonlinearity required for entanglement generation.

At the level of an effective description, the total Hamiltonian governing a neutral-atom two-qubit gate can be written as

$$\hat{H}_{\text{tot}}(t) = \hat{H}_{\text{Gr-Ryd}}(t) + \hat{H}_{\text{Ryd}}, \quad (1)$$

where $\hat{H}_{\text{Gr-Ryd}}(t)$ describes optical coupling between the computational states and Rydberg levels and \hat{H}_{Ryd} accounts for the interactions between Rydberg excitations on different atoms.

A CZ Rydberg gate consists of a pair of atoms, where one is the control atom (denoted by C) and the other being the target atom (denoted by T). In each of these atoms, a set of N_{Ryd} Rydberg states $\{|r_{ia}\rangle \mid 1 \leq i \leq N_{\text{Ryd}}\}$ can be accessed via laser excitation from the computational state $|1\rangle_a$ with $a \in \{C, T\}$. The Rydberg interaction Hamiltonian reads

$$\hat{H}_{\text{Ryd}} = \frac{1}{2} \sum_{i,j,k,l=1}^{N_{\text{Ryd}}} \langle r_{iC} r_{jT} | \hat{V}_{dd} | r_{kC} r_{lT} \rangle |r_{iC} r_{jT}\rangle \langle r_{kC} r_{lT}|. \quad (2)$$

The laser coupling Hamiltonian takes the form

$$\hat{H}_{\text{Gr-Ryd}}(t) = \sum_{a=C,T} \sum_{i=1}^{N_{\text{Ryd}}} \frac{\Omega_{ia}(t)}{2} e^{i\varphi_{ia}(t)} |1\rangle \langle r_{ia}|_a + \text{h.c.}, \quad (3)$$

where $\Omega_{ij,a}^{\text{mw}}(t)$'s are the microwave drive Rabi pulses coupling Rydberg states $|r_{ia}\rangle$ and $|r_{ja}\rangle$ of atom $a=C, T$, and $\varphi_{ij,a}^{\text{mw}}(t)$ their corresponding phases.

The interaction Hamiltonian \hat{H}_{Ryd} depends on the specific gate mechanism and encodes the van der Waals or resonant dipole-dipole interactions between Rydberg excitations on the control and target atoms.

A. Blockade gates

Rydberg atoms possess large electric dipole moments and polarizabilities, leading to strong, long-range interactions at micrometer-scale separations. These gates exploit the strong van der Waals interaction between two identical Rydberg states to suppress simultaneous excitation of both atoms and thereby generate conditional dynamics. Shortly after their introduction [35], the idea to harness Rydberg blockade for performing task relevant for quantum computation was extended to mesoscopic ensembles, emphasizing its scalability, robustness, and applicability to quantum computing.

In the simplest realization, a single Rydberg state $|r\rangle$ is involved for both atoms, whose van der Waals interaction implements the required correlations. The corresponding Rydberg interaction Hamiltonian is

$$\hat{H}_{\text{Ryd-Blockade}} = V(R) |rr\rangle \langle rr|_{CT}, \quad (4)$$

where $V(R) = C_6/R^6$ is the van der Waals interaction potential, R is the interatomic separation, and C_6 is the van der Waals coefficient associated with the Rydberg state $|r\rangle$, see Fig. 1(b).

The blockade is a mature entangling mechanism in neutral-atom platforms, with well-established theoretical models, benchmarks, and experimental demonstrations [35, 45–47]. Gate durations can be made short

compared to ground state coherence times and the rate of various kinds of errors [44, 48], reducing sensitivity to technical noise sources and fundamental limitations of the dynamics, such as spontaneous emission or unwanted admixture with other Rydberg states [64].

In practice, the blockade interaction is always finite, leading to residual population of Rydberg excitations and leakage errors when the Rabi frequency is not negligible compared to the interaction shift. Furthermore, a well-known limitation of blockade gates arises from residual population in the Rydberg excited state $|rr\rangle$. Because the van der Waals interaction has a $1/R^6$ distance dependence, residual population in doubly excited Rydberg states produces forces that couple internal states to atomic motion, degrading gate fidelity. This population experiences a force $F(R) = -\partial_R V(R)$, which couples the internal Rydberg excitation to the relative motional degree of freedom of the atoms. As a consequence, atomic motion becomes entangled with the internal states, leading to motional decoherence and a reduction of gate fidelity, particularly in shallow or finite-temperature optical tweezers. The required small distance between the atoms required for high-fidelity blockade gates to be within a well-defined blockade radius, constrains the array geometry and limits interaction selectivity in dense systems.

B. Non-blockade and dark state-based gates

Beyond blockade-based schemes, several alternative two-qubit gate proposals have been developed (e.g., Refs. [43, 49]). Several non-blockade based gates are based on the geometric phase [55, 57, 58]. Many non-blockade schemes engineer entanglement through states whose energies are weakly dependent (or independent) of interatomic separation, mitigating force-induced motional entanglement that plagues the blockade gates.

Among the most promising of these is the *two-atom dark state gate* [43], in which entanglement is generated through adiabatic evolution of a collective dark state. By exploiting interference, adiabatic elimination, or dark states, these gates keep the population of $|rr\rangle$ small, reducing both Rydberg decay and mechanical forces.

A key advantage of the dark state approach is that the relevant eigenstate is, to leading order, insensitive to the interatomic separation. As a result, population in the doubly excited Rydberg manifold is strongly suppressed throughout the gate, mitigating motional decoherence and improving robustness against atomic motion.

The dark state gate involves two Rydberg states $|r_C\rangle_C$ and $|r_T\rangle_T$, which may be identical or different for the control and target atoms, see Fig. 1(a) and (c). The doubly excited state $|r_{CRT}\rangle$ is resonantly or near-resonantly coupled to another pair of Rydberg states $|r_{+,C} r_{-,T}\rangle_{CT}$ via a Förster interaction satisfying

$$E(r_C) + E(r_T) + \Delta = E(r_{+,C}) + E(r_{-,T}), \quad (5)$$

where Δ is the Förster defect. Hereafter, we assume resonant interactions where $\Delta = 0$ with the application of a constant electric field to Stark-tune the resonance, see Fig. 1(a). Without loss of generality, we assume $|r_C r_T\rangle$ is coupled to $|r_{+,C} r_{-,T}\rangle$.

In the case of identical Rydberg states, $r_C = r_T = r$, the state $|rr\rangle$ couples to the symmetric combination

$$|(r+r_-)\rangle = \frac{1}{\sqrt{2}} [|r+r_-\rangle + |r-r_+\rangle].$$

where circular brackets indicate symmetric combination. The Rydberg interaction Hamiltonian in this case takes the form

$$\begin{aligned} \hat{H}_{\text{Ryd-Förster}} = & -\Delta |rr\rangle\langle rr| \\ & + [B(R) |(r+r_-)\rangle\langle rr| + \text{h.c.}] , \end{aligned} \quad (6)$$

where $B(R)$ is the dipole-dipole coupling strength, scaling as $B(R) \sim R^{-3}$, see Fig. 1(a) and (c).

C. Driving scheme and invariant subspaces

We consider a standard local addressing scheme in which each atom is driven independently by laser pulses coupling $|1\rangle_a$ to $|r_a\rangle$ with Rabi frequency $\Omega_a(t)$ and phase $\varphi_a(t)$ (since here we consider only one single Rabi coupling, we have dropped the index i labeling the Rydberg levels).

The dynamics generated by $\hat{H}_{\text{tot}}(t)$ decomposes into invariant subspaces of the total Hilbert space $\mathcal{H} = \bigoplus_{q \in \{0,1\}^2} \mathcal{H}_q$, where

$$\mathcal{H}_q = \{|p_C p_T\rangle_{CT} \mid p_a \in \{0, 1, r_a\}, p_a = q_a \text{ if } q_a = 0\}.$$

Accordingly, the time-evolution operator decomposes as $\hat{U}(t) = \bigoplus_q \hat{U}_q(t)$ [44]. The subspace \mathcal{H}_{00} is trivial, while \mathcal{H}_{01} and \mathcal{H}_{10} correspond to single-qubit dynamics. The entangling dynamics occurs in

$$\mathcal{H}_{11, \text{Blockade}} = \text{Span}\{|11\rangle, |1r\rangle, |r1\rangle, |rr\rangle\}, \quad (7)$$

$$\mathcal{H}_{11, \text{DarkState}} = \text{Span}\{|11\rangle, |1r\rangle, |r1\rangle, |rr\rangle, |(r+r_-)\rangle\}. \quad (8)$$

As shown in Ref. [65], the instantaneous eigenstates of the dark state Hamiltonian $\hat{H}_{\text{DarkState}} = \hat{H}_{\text{laser}}(t) + \hat{H}_{\text{Ryd-Forster}}$ exhibit admixtures of bright states that scale as $(\Omega_{\text{max}}/B)^2$. The exact spectrum of the dark state gate's Hamiltonian [65] therefore predict a strong suppression of sensitivity to motional fluctuations compared to blockade gates. In the following, we first discuss pulse sequence designs to implement CZ gates via blockade and adiabatic dark state schemes, and then apply quantum optimal control to obtain non-adiabatic preparation of dark state gates. After that we analyze and compare the response of the blockade as well as the adiabatic and non-adiabatic dark state gates to dominant experimental error sources, including atomic motion in optical tweezers, laser phase and intensity noise, and finite Rydberg-state lifetimes.

III. DESIGN OF PULSE SEQUENCES

A gate design problem reduces to finding a suitable level scheme and pulse sequences which drive coherent state transfer between the considered states such that at the end of the pulse sequence, the desired unitary operator corresponding to the gate operation is implemented. Here we discuss two prominent methods to obtain pulse sequences for the implementation of CZ gates.

A figure of merit to analyze the performance of two-qubit gates is the trace fidelity

$$F = \left| \frac{1}{d} \text{Tr}(\hat{U}_{\text{target}}^\dagger \hat{U}(T)) \right|^2, \quad (9)$$

where \hat{U}_{target} ($\hat{U}(T)$) stands for the target unitary (the implemented unitary). The fidelity error is then defined by $\varepsilon = 1 - F$.

The target unitary for a CZ gate takes the form $\hat{U}_{\text{target}} = \text{diag}(1, e^{i\theta_1}, e^{i\theta_2}, e^{i(\theta_1+\theta_2+\pi)})$ in the computational basis $\{|00\rangle, |01\rangle, |10\rangle, |11\rangle\}$. Here, θ_1 and θ_2 are arbitrary single-qubit phases gained by the qubit state $|1\rangle$ relative to $|0\rangle$, and the gate is diagonal in the computational basis. Here we discuss two methods for obtaining such pulses. First, we describe the $\pi - 2\pi - \pi$ sequence, which was used in the original proposal [45] and is considered in the main work introducing the dark state gate [43]. Then, we apply QOC to obtain to find optimal pulses to implement the non-adiabatic dark state CZ gate.

A. $\pi - 2\pi - \pi$ sequence

The $\pi - 2\pi - \pi$ pulse was the first pulse shape proposed to implement the CZ gate. It works by (i) applying a π pulse to bring the state $|11\rangle$ to $-i|r1\rangle$, (ii) applying a 2π pulse on the target qubit to bring the state $-i|r1\rangle$ to $-i|r1\rangle$ (since the Rabi oscillation is suppressed due to the Rydberg blockade), and (iii) applying a final π pulse on the control qubit to bring $-i|r1\rangle$ to $-|11\rangle$. It can be shown that this pulse sequence maps $|00\rangle \rightarrow |00\rangle$, $|01\rangle \rightarrow -|01\rangle$ and $|10\rangle \rightarrow -|10\rangle$, thus it implements a CZ phase up to a π single qubit phase of states $|1\rangle$. The adiabatic version of this protocol was considered in Ref. [43] to implement an adiabatic dark state gate. Here, instead of the strong Rydberg blockade, the evolution of the adiabatic state over the zero energy dark state leads to a vanishing phase accrual at step (ii), thus implementing the same gate.

Here we consider smooth Rabi coupling pulse shapes for the target and control qubits, of the form

$$\Omega(t) = \Omega_{\text{max}} \left[b(T/\sigma) - a(T/\sigma) \left(e^{-t^2/2\sigma^2} + e^{-(t-T)^2/2\sigma^2} \right) \right], \quad (10)$$

where $a(x) = 1/(1 + e^{-x^2/2} + e^{-x^2/8})$, $b(x) = (1 + e^{-x^2/2})/(1 + e^{-x^2/2} + e^{-x^2/8})$, Ω_{\max} is the maximum Rabi frequency, T is the duration that implements a pulse with pulse area Θ and is obtained from

$$T\Omega_{\max} = \frac{\Theta}{b(T/\sigma) - \sqrt{2\pi}(\sigma/T)a(T/\sigma)\text{erf}(T/\sqrt{2}\sigma)}, \quad (11)$$

with $\text{erf}(x) = 2/\sqrt{\pi} \int_0^x dt e^{-t^2/2}$. The ratio σ/T controls how smoothly the Rabi pulse reaches the maximum value Ω_{\max} , which we set to $\sigma/T = 0.05$. These pulse forms are used in the original proposal [43] and are depicted in the inset of Fig. 1(a).

In the original implementation of the dark state gate, the Rabi pulses are adiabatic, such that the instantaneous eigenstates in step (ii) follows adiabatically the two-atom dark state $|D(t)\rangle = 1/\sqrt{B^2 + \Omega_T^2(t)/4} [B|r,1\rangle - \Omega_T/2|r+r-\rangle]$. In this way, the population of the $|rr\rangle$ state is suppressed and the force due to the van der Waals interaction is mitigated. However, non-adiabaticity can result in a finite population of $|rr\rangle$, which affects the gate performance.

B. Application of QOC: the non-adiabatic dark state CZ gate

Quantum optimal control has previously been applied to the design of time optimal entangling gates, most notably in Ref. [44], where high fidelity time optimal blockade CZ gates were realized. In contrast, its application to dark-state gate schemes has not been explored prior to the present work. To this end, a well-established gradient-based optimization algorithm is the GRadient Ascent Pulse Engineering (GRAPE). To find pulses that implement high-fidelity gates, the control signals consist of the Rabi couplings of the control and target qubits $\Omega_{C,T}(t)$, and their phases $\varphi_{C,T}(t)$. Fixing an implementation time T , time is then discretized into N equal length intervals $\delta t = T/N$ with discrete points $t_k = k\delta t$, $k = 0, 1, 2, \dots, N$ with $t_0 = 0$ and $t_N = T$. The time evolution unitary is then implemented as $\hat{U}(T) = \prod_{k=0}^{N-1} \hat{U}(t_{k+1}, t_k)$ where $\hat{U}(t_{k+1}, t_k) = \mathcal{T}\{\exp(-i/\hbar \int_{t_k}^{t_{k+1}} d\tau \hat{H}(\tau))\}$. In the $[t_k, t_{k+1}]$ interval, the control signals are assumed to be constant $\Omega_{C,T}(t) = \Omega_{C,T}(t_k)$, $\varphi_{C,T}(t) = \varphi_{C,T}(t_k)$, $t \in [t_k, t_{k+1}]$, and the Hamiltonian in the k 'th time interval becomes only a function of these control signals. The cost function for the optimization is the fidelity error ε which is a function of all the control signals, $\varepsilon\{\{\Omega_{C,T}[k]\}_{k=0}^N, \{\varphi_{C,T}[k]\}_{k=0}^N\}$, which can be minimized using a gradient-based optimization algorithm, where the L-BFGS-B algorithm is often used. Here we use the Python implementation of L-BFGS-B using the function `scipy.optimize.minimize`. To obtain time optimal pulses, the fixed gate time T is reduced and optimal pulses which implement high-fidelity gates are obtained until a sharp increase in error is found.

Here, we apply quantum optimal control using GRAPE to find time-optimal pulses for both the blockade and the dark state gate. The pulses obtained for the dark state gate goes beyond the adiabatic dark state gate (Ad dark state), resulting in the *non-adiabatic dark state* (NAd dark state) gate. To benchmark the performance of each gate, we consider an experimentally relevant setup consisting of ^{133}Cs atoms, with the Rydberg state $|r\rangle = |nP_{3/2}, m_j=3/2\rangle$, which can be tuned to a Förster resonance with the states $|r_-\rangle = |nS_{1/2}, m_j=1/2\rangle$ and $|r_+\rangle = |(n+1)S_{1/2}, m_j=1/2\rangle$. We use the `PairInteraction` package [66] to find the interaction strengths, decay rates of the states and other relevant system parameters. We assume a magnetic field $B_z = 100\text{ G}$ where the quantization axis is taken to be the z direction, while the interatomic distance is orthogonal to the quantization axis, which we take to be the x direction. For the blockade gate, the Rydberg state interaction is realized via the off-resonant van der Waals interaction at the applied electric field $E_z = 0$, while setting the electric field to the Förster resonance $E_z = E_{\text{res}}$ allows for the implementation of the dark state gate. Here, we take the $n = 70$ Rydberg state of ^{133}Cs , which has a blockade radius $R_B \simeq 4.6\text{ }\mu\text{m}$ at $\Omega_{\max} = 2\pi \times 10\text{ MHz}$.

Applying quantum optimal control to both the blockade gate and the dark state gate, we find that at the minimal gate implementation time, $\Omega_C(t) = \Omega_T(t) = \Omega_{\max}$, and $\varphi_C(t) = \varphi_T(t)$, see Fig. 1(b,c). This observation is consistent with the earlier findings [44] that the time optimal blockade gate is realized for global pulses with constant Rabi frequencies equal to the maximum achievable Rabi frequency. The infidelities for different gate times and distances for the two atoms are shown in Fig. 2.

We find that at small distances within the blockade radius, the non-adiabatic dark state gate performs similar to the blockade gate, specifically, the minimum implementation time for both gates approach $T_{\text{opt}} \Omega_{\max}/2\pi \simeq 1.2113$, which is the value obtained for the time optimal blockade gate in the limit $V_{\text{vdW}} \rightarrow \infty$ in Ref. [44]. The existence of such a limiting value reflects the fact that the optimal control solution obeys a minimum-action principle, as encapsulated by Pontryagin's maximum principle. This behavior has been explicitly demonstrated for the time-optimal ideal blockade gate in Ref. [44].

To explain this effect, we note that the Hamiltonian of the gate G (G being either the blockade or the non-adiabatic dark state gate) in the subspace \mathcal{H}_{11} can be cast into the block form

$$\hat{H}_G(t) = \begin{bmatrix} \hat{H}_{\text{ideal}}(t) & \hat{V}(t) \\ \hat{V}(t)^\dagger & \hat{H}_H \end{bmatrix}, \quad (12)$$

where $\hat{H}_{\text{ideal}}(t)$ is the Hamiltonian of an *ideal blockade* gate, that is a blockade gate with $V_{\text{vdW}} \rightarrow \infty$, which acts in the reduced subspace $\bar{\mathcal{H}}_{11} = \text{Span}\{|11\rangle, |1r\rangle, |r1\rangle\}$, $\hat{V}(t)$ is the coupling between the states in $\bar{\mathcal{H}}_{11}$ to the high-energy Rydberg subspace \mathcal{H}_H , which for the van der Waals gate is $\mathcal{H}_{H,\text{vdW}} = \text{Span}\{|rr\rangle\}$ and for the dark

state gate $\mathcal{H}_{H,\text{DarkState}} = \text{Span}\{|rr\rangle, |(r+r_-)\rangle\}$. The projected Hamiltonian into the high-energy subspace $\hat{H}_H(t)$ describes the Rydberg state interactions, thus $\hat{H}_H = \hat{H}_{\text{Ryd-Blockade}}$ ($\hat{H}_H = \hat{H}_{\text{Ryd-Förster}}$) for the blockade (dark state) gates. In both cases, an effective Hamiltonian for the dynamics in the reduced subspace $\bar{\mathcal{H}}_{11}$ can be obtained using the Schrieffer-Wolf transformation [65].

$$\hat{H}_{\text{eff},G}(t) = \hat{H}_{\text{ideal}}(t) + \sum_{N=1}^{\infty} \delta\hat{H}_G^{(N)}(t), \quad (13)$$

with $\delta\hat{H}_G^{(N)}(t)$ the N 'th order term in $\hat{V}(t)$ in the perturbative expansion. Accordingly, the time evolution operator $\hat{U}_{11}(t)$ in the \mathcal{H}_{11} subspace can be expressed as $\hat{U}_{11}(t) = \hat{U}_{11,\text{ideal}}(t)[\mathbb{I} + \delta\hat{U}_{11,G}(t)]$, where $\delta\hat{U}_{11,G}(t)$ is generated by the terms $\delta\hat{H}_G^{(N)}(t)$. Utilizing the separability of the dynamics as explained in Sec. II C, the whole time evolution operator takes the form

$$\hat{U}(t) = \bigoplus_{q \in \{0,1\}^2} \hat{U}_{q,\text{ideal}}(t)[\mathbb{I} + \delta\hat{U}_{q,G}(t)], \quad (14)$$

with $\delta\hat{U}_{q,G}(t) = \delta\hat{U}_{11,G}(t)$ if $q = (1, 1)$ and $\delta\hat{U}_{q,G}(t) = 0$ otherwise. The error infidelity for the gate G also has a perturbative expansion as

$$\begin{aligned} \varepsilon_G &= 1 - \left| \frac{1}{d} \text{Tr} \left(\hat{U}_{\text{target}}^\dagger \hat{U}_{\text{ideal}}(T) [\mathbb{I} + \delta\hat{U}_G(T)] \right) \right|^2 \\ &= \varepsilon_{G,\text{ideal}} + \delta\varepsilon_G, \end{aligned} \quad (15)$$

with $\varepsilon_{G,\text{ideal}} = |1/d \text{Tr}(\hat{U}_{\text{target}}^\dagger \hat{U}_{\text{ideal}}(T))|^2$, and $\delta\varepsilon_G$ are the corrections due to $\delta\hat{U}_G(T)$. For the limit $R \rightarrow 0$, $V(R), B(R) \rightarrow \infty$, thus the functional form of the fidelity error for both gates which is the cost function in the optimization reduces to the one for the ideal blockade gate. This explains the observed behavior of the infidelity in the limit $R \rightarrow 0$ of both gates.

As the interatomic distance approaches the blockade radius $R_B \sim 4.5 \mu\text{m}$, the blockade gate rapidly loses fidelity, while the dark state gate still maintains high fidelities while the gate implementation time remains of close to the optimal time, $T \simeq T_{\text{opt}}$. This observation is understood by the rapid decrease in the van der Waals interaction strength by its R^{-6} scaling compared to the resonant dipole-dipole interaction strength, which scales as R^{-3} , see Fig. 1.

These results demonstrate that the non-adiabatic dark state protocol obtained via QOC retains the intrinsic robustness of adiabatic dark state gates against reduced interaction strengths and increased interatomic spacing, while simultaneously overcoming their known limitation of long gate times. In this way, the optimized non-adiabatic dark state gate combines the favorable distance scaling and robustness of dark state schemes with gate speeds comparable to those of time optimal blockade

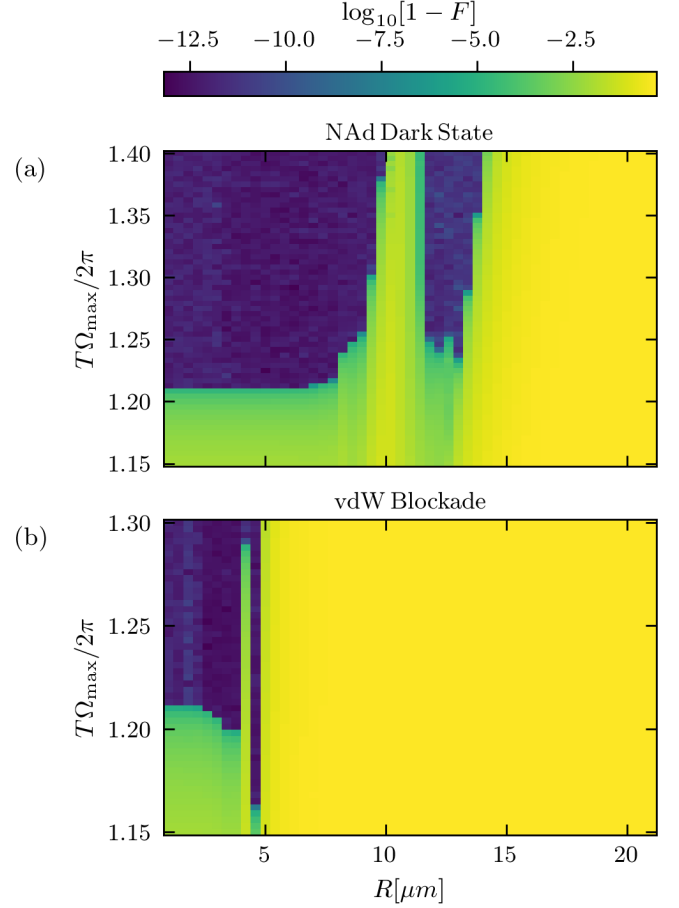


FIG. 2. Fidelity error for the CZ gate as a function of interatomic distance R and implementation time T (in units of $2\pi/\Omega_{\text{max}}$) for (a) the non-adiabatic dark state gate, and (b) for the blockade gate. To implement the dark state gate, an electric field $E_z = E_{\text{res}}$ is applied in the quantization direction z , to bring the two-atom Rydberg state $|rr\rangle$ into resonance with $|(r+r_-)\rangle$ via Stark tuning. The resonant Rydberg states are $|r\rangle = |70P_{3/2}, m_j=3/2\rangle$, $|r_+\rangle = |71S_{1/2}, m_j=1/2\rangle$ and $|r_-\rangle = |70S_{1/2}, m_j=1/2\rangle$. For the limit $R \rightarrow 0$, the minimum implementation time approaches the optimal time $T_{\text{opt}} \simeq 1.2113 \cdot 2\pi/\Omega_{\text{max}}$ for the ideal blockade gate ($\Omega_{\text{max}} = 2\pi \times 10 \text{ MHz}$), i. e. the van der Waals block gate with $V_{\text{vdW}} \rightarrow \infty$. As the blockade radius $R_B \simeq 4.6 \mu\text{m}$ is approached, the blockade gate rapidly loses performance, while the non-adiabatic dark state gate still maintains high fidelity for implementation times T comparable to T_{opt} at distances $R \sim 10 \mu\text{m}$.

gates, enabling high fidelity operation beyond the conventional blockade radius.

Having established the superior performance of the non-adiabatic dark state gate at longer distances compared to the blockade gate, an important question remains: how susceptible is the non-adiabatic dark state gate compared to its adiabatic counterpart and to the blockade gate to the coupling of the Rydberg excitation to atomic motion? This question is critical since the non-

adiabatic protocol increases the contribution of the $|rr\rangle$ state in the gate dynamics, thus it is expected that the resulting van der Waals force would be more prominent and more strongly affects the gate performance. In the next section, we analyze the response of the two variations of the dark state gate to atomic motion and compare it to the blockade gate.

IV. COMPARATIVE ERROR ANALYSIS FOR THE NON-ADIABATIC DARK STATE GATE

In the remainder of this work, we focus on the comparison of the non-adiabatic gate performance to its adiabatic counterpart and the blockade gate in terms of other prominent error sources, namely the decoherence due to the coupling of Rydberg excitations to the atomic motion, the decay of Rydberg states, and the influence of the phase and amplitude noise.

A. Influence of the internal-motional coupling on the gate performance

The coupling of the internal degrees of freedom with the atomic motion is a significant source of error in the implementation of quantum gates with Rydberg atoms [26, 49, 67, 68]. The effect of internal-motional coupling on the dynamics of the Rydberg systems have been studied in detail for applications in quantum simulation and many-body physics [69–74]. Thus, understanding the dynamics of these systems and the influence of this coupling in the performance of the quantum engineered systems and devising methods to mitigate the resulting errors is of key interest in these fields.

In the context of two-qubit gates, the quantum fluctuations of the atomic positions inside the tweezer traps couple to Rydberg excitations via the resulting induced changes in the Rydberg interaction strength, as well as sampling the electric field of the driving laser at different positions. The former effect is responsible for causing an effective force between the two atoms, while the latter results in a position-fluctuation induced random phase of the Rydberg transition, which can also be described in terms of photon recoil [49].

Here we focus on a configuration similar to Ref. [49] where the excitation laser propagates along the interatomic axis, which we take to be the x axis. For every phonon number state of the motional degree of freedom of each atom within the trap, $|n_a\rangle$, $n_a = 0, 1, \dots$, the infidelity is calculated by time-evolving the total internal-motional state according to the total Hamiltonian in Ref. [49] and then averaging over the thermal phonon distribution at a certain temperature T and trap frequency ω_x . The resulting calculated infidelities due to the coupling to the thermal motion for $T_{\text{th}} = 1 \mu\text{K}$ and trap frequencies $\omega_x = 50 \text{ kHz}$ is shown in Table. I. The principal quantum number of the Rydberg excitation is $n = 70$,

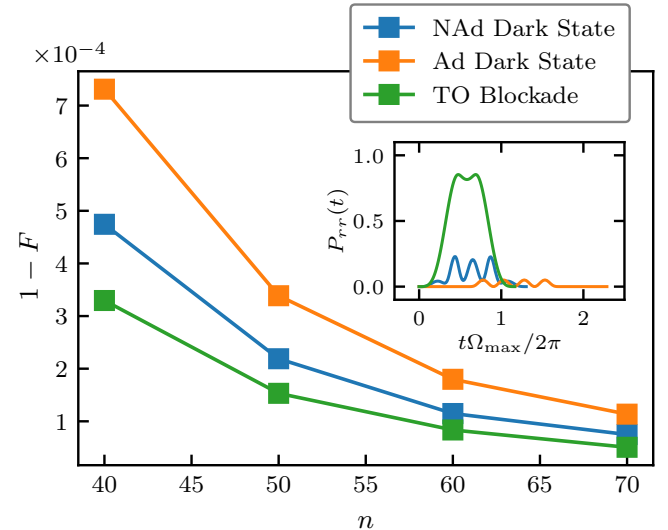


FIG. 3. CZ gate error due to Rydberg state decay, as a function of the principal quantum number n , for the non-adiabatic dark state (blue), adiabatic dark state (orange) and the blockade (green) gates. The inset shows the time dependence of the doubly excited Rydberg state population $P_{rr}(t)$. The non-adiabaticity increases the Rydberg state population during the gate time evolution for the non-adiabatic dark state gate compared to its adiabatic counterpart. However, the unwanted population is still significantly smaller than the blockade gate. However, due to the larger decay rate of the $S_{1/2}$ states of the ^{133}C atom compared to the $P_{3/2}$ states, the decay error is largest for the adiabatic dark state and the smallest for the time optimal blockade, with the non-adiabatic dark state gate in between. Compared to the adiabatic dark state gate, the non-adiabatic version shows increased performance.

and the gates are compared at a distance $R \simeq 4.2 \mu\text{m}$, where all gates demonstrate high fidelity ($\varepsilon < 10^{-10}$). Surprisingly, the non-adiabatic gate shows the least fidelity error, $\varepsilon_{\text{NAd}} \simeq 1.11 \times 10^{-5}$, which is smaller than the adiabatic counterpart with $\varepsilon_{\text{Ad}} \simeq 4.00 \times 10^{-5}$. This counterintuitive effect can be attributed to the competition between the unwanted population of $|rr\rangle$ state due to non-adiabaticity, and the total gate duration time, which increases the error rate. Here, while the non-adiabatic dynamics increases the population of the undesired Rydberg state, the shorter gate duration time leads to a smaller error compared to the adiabatic gate which implements the gate more slowly. Furthermore, both types of the dark state gate demonstrate higher fidelities as compared to the blockade gate, although the implementation of the blockade gate possess time optimality. This lower fidelity error highlights the potential of non-adiabatic dark state gate and the promise of dark state gates for achieving better performance compared to the blockade gates by application of quantum optimal control methods.

B. Errors due to the Rydberg decay

Spontaneous emission of Rydberg states together with their vulnerability to black-body radiation are known to be major error sources in quantum hardware due to neutral atoms **cite**. Here we also examine the fidelity of the three types of gates with respect to the decay of Rydberg states. To this end, we consider the addition of the non-hermitian decay terms to the Hamiltonian,

$$\hat{H}_{\text{Decay}}(t) = \hat{H}_{\text{tot}}(t) - \sum_{a=C,T} \sum_{j=1}^{N_{\text{Ryd}}} \frac{i\hbar\Gamma_{ja}}{2} |r_{ja}\rangle\langle r_{ja}|_a, \quad (16)$$

where Γ_{ja} is the decay rate of the Rydberg state j of atom a , see Ref. [65] for the numerical values. Application of this non-hermitian evolution is sufficient here since the dynamics happens in the Fermi golden rule regime as a result of the slow decay rate of the Rydberg states compared to the time scale of the gate dynamics. The non-unitary contracting time evolution operator $\hat{U}_{\text{Decay}}(t)$ according to $\hat{H}_{\text{Decay}}(t)$ results in the infidelity $\varepsilon = 1 - F$, where $F = |(1/d)\text{Tr}(\hat{U}_{\text{target}}^\dagger \hat{U}_{\text{Decay}}(t))|^2$.

The resulting errors are depicted in Fig. 3. A decisive quantity which explains the behavior of the observed fidelity error is the doubly excited Rydberg state population

$$P_{rr}(t) = \langle \psi(t) | \hat{\Pi}_{rr} | \psi(t) \rangle, \quad (17)$$

where $\hat{\Pi}_{rr} = |rr\rangle\langle rr|$ is the projector on the $|rr\rangle$ state. While the Rydberg state population in the $|rr\rangle$ state is increased for the non-adiabatic gate as compared to its adiabatic counterpart as a result of non-adiabaticity, the gate error is smaller for all values of the principal quantum number n . This result can be attributed to the larger decay rate of the $nS_{1/2}$ and $(n+1)S_{1/2}$ states of ^{133}Cs compared to the $nP_{3/2}$ state for the n values considered (see Ref. [65]). On the other hand, although the $|rr\rangle$ state population is the largest during the blockade gate dynamics, the resulting error is less than for both dark state gates, again due to the absence of population in the $|(r_+r_-)\rangle$ state.

In conclusion, while the non-adiabatic dark state gate shows increased error compared to the blockade gate due to population of the $|(r_+r_-)\rangle$ state with decay rate larger than $|rr\rangle$, it outperforms its adiabatic counterpart, since the adiabatic gate is implemented over a longer duration. Recently, quantum optimal control also has been applied to saturate with a few percent a fundamental bound on the decay due to error [43], which highlights the utility of quantum optimal control techniques to improve various aspects of the dark state gate performance.

C. Fidelity error due to the laser frequency noise

Aside from the aforementioned error sources, fluctuations in the laser frequency noise is known to be another

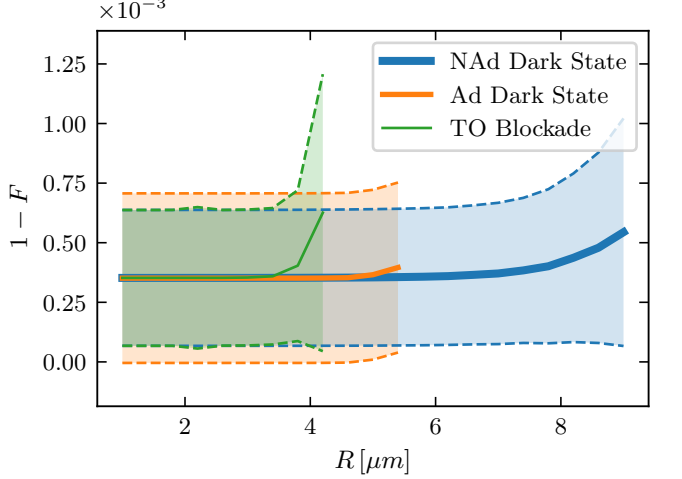


FIG. 4. Mean infidelity due to laser phase fluctuations (thick solid lines) for the non-adiabatic dark state gate (blue) and the blockade gate (orange). The regions within one standard deviation is highlighted for each gate. While at distances $R \lesssim 3 \mu\text{m}$ all gates have similar fidelity errors, the blockade gate rapidly loses fidelity around $R \simeq 4 \mu\text{m}$, while the non-adiabatic dark state gate maintains a reasonable performance up to $R \simeq 8 \mu\text{m}$.

major source of error. The frequency fluctuations directly translates into the Rabi phase fluctuations. Thus, studying the influence of the phase fluctuation is also of prime importance to quantify the gate performance.

To this end, \mathcal{N} random phase time traces $\delta\varphi_a^{(i)}(t)$, $i = 1, \dots, \mathcal{N}$ is created for atom a according to the single-side-band power spectral density of the laser phase noise [65]. The noise samples are then added to the pulse obtained by quantum optimal control $\varphi_{a,\text{opt}}(t)$ to obtain noisy phase pulse time traces $\varphi_a^{(i)}(t) = \varphi_{a,\text{opt}}(t) + \delta\varphi_a^{(i)}(t)$. The obtained infidelities $\varepsilon_{\text{phase}}^{(i)} = \varepsilon[\{\Omega_{a,\text{opt}}(t), \varphi_a^{(i)}(t)\}_{a=C,T}]$ form a sequence of random phase errors with mean $\bar{\varepsilon}_{\text{phase}} = 1/\mathcal{N} \sum_{i=1}^{\mathcal{N}} \varepsilon_{\text{phase}}^{(i)}$ and standard deviation $\sigma_{\text{phase}}^2 = \sum_{i=1}^{\mathcal{N}} (\varepsilon_{\text{phase}}^{(i)} - \bar{\varepsilon}_{\text{phase}})^2 / (\mathcal{N} - 1)$. The mean error and its variance are depicted in Fig. 4 for the three type of gates considered in this work for various distances. It is observed that in the $R \rightarrow 0$ limit, all gates reach the ideal blockade noise response.

As the blockade radius is approached, the blockade gate shows increasing susceptibility to noise, whereby both the mean fidelity error and its variance increase. On the other hand, the adiabatic dark-state gate exhibits greater robustness to variations in the interatomic distance, while its performance gradually degrades with increasing separation and eventually drops sharply at the largest distance considered ($R_B \lesssim R$ in Fig. 4 in the atomic distance). The non-adiabatic gate demonstrates the best robustness against the noise: while in the blockade regime, the fidelity error statistics closely follows that

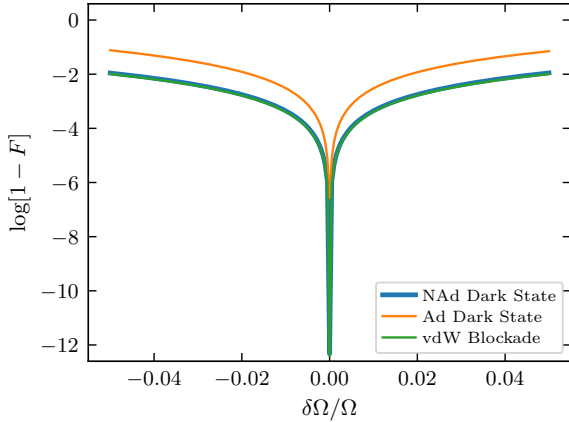


FIG. 5. Infidelity due to the shot-to-shot intensity noise, for the non-adiabatic dark state (blue), adiabatic dark state (orange), and the blockade gate (green). The performance of the non-adiabatic dark state gate is enhanced compared to the adiabatic dark state gate and becomes comparable to the blockade gate.

of the blockade gate, it sustains over distances $R \simeq 8 \mu\text{m}$, where eventually the non-adiabatic dark state gate starts to deteriorate. This result also demonstrates the enhanced performance in terms of phase noise resilience of the non-adiabatic gate compared to both the blockade and the adiabatic dark state gate.

D. Fidelity error due to the laser intensity noise

The last error source we consider is the shot-to-shot laser intensity fluctuations. The effect of this error source is modeled by obtaining the infidelity as a function of the change in Rabi frequency Ω_a by $\delta\Omega_a$ which, due to its low frequency can be taken as constant during the application of the gate [26, 75].

The resulting error for different gates are depicted in Fig. 5, where it can be inferred that the non-adiabatic dark state gate performs similarly to the blockade gate due to the intensity fluctuations, while both gates are more robust compared to the adiabatic dark state gate. The adiabatic dark state gate is known to be sensitive to the fluctuations in the Rabi frequency, as it causes a remaining population in the Rydberg states after the application of the gate [43]. We conclude that the performance of the dark state gate in response to intensity fluctuations can be enhanced by application of quantum optimal control to make the gate non-adiabatic.

V. CONCLUSION AND OUTLOOK

We applied quantum optimal control to design high-fidelity, time-optimal pulses for the Rydberg dark state gate, originally introduced as an adiabatic protocol [43], and performed a systematic, quantitative comparison with standard blockade-based gate implementations. The resulting non-adiabatic dark state gate retains the robustness to variations in interatomic distance characteristic of the dark state mechanism and the long-range resonant dipole-dipole interaction, while outperforming the adiabatic gate in response to Rydberg state decay and laser amplitude and phase fluctuations. Its performance in decay error approaches that of the blockade gate, while it matches or exceeds the blockade gate for noise and distance robustness. These results demonstrate, through a unified and systematic analysis, that quantum optimal control can systematically enhance the speed, fidelity, and resilience of dark-state gates.

As an outlook, it would be interesting to examine in more detail the interplay between implementation time, non-adiabaticity, and Rydberg state population, and how this competition influences gate fidelity. Another important direction is to develop control schemes that render the gates robust against Förster defect fluctuations, internal-motional coupling, the residual van der Waal interaction of the $|rr\rangle$ state and laser crosstalk for the case of different control and target Rydberg states, extending the applicability of dark state gates in realistic conditions. Designing robust pulses for longer interatomic distances could mitigate errors arising from motional states, potentially increasing the gate range while preserving high fidelity. Furthermore, exploring the effects of different excitation directions on reducing the effect of atomic motion will further illuminate the limitations and opportunities for optimizing gate performance.

VI. ACKNOWLEDGMENT

This work is funded by the German Federal Ministry of Education and Research within the funding program “Quantum Technologies - from basic research to market” under Contract No. 13N16138. R.M. acknowledges support from the U.S. National Institute of Standards and Technology (NIST) through the CIPP program under Award No. 60NANB24D218. and the U.S. National Science Foundation (NSF) through the NSF TIP program under Award No. 2534232.

[1] R. N. Tazhigulov, S.-N. Sun, R. Haghshenas, H. Zhai, A. T. Tan, N. C. Rubin, R. Babbush, A. J. Minnich, and G. K.-L. Chan, Simulating models of challenging corre-

lated molecules and materials on the sycamore quantum processor, *PRX Quantum* **3**, 040318 (2022).

[2] C. Cao, J. Sun, X. Yuan, H.-S. Hu, H. Q. Pham, and D. Lv, Ab initio quantum simulation of strongly correlated materials with quantum embedding, *npj Comput. Mater.* **9**, 78 (2023).

[3] L. Clinton, T. Cubitt, B. Flynn, F. M. Gambetta, J. Klassen, A. Montanaro, S. Piddock, R. A. Santos, and E. Sheridan, Towards near-term quantum simulation of materials, *Nat. Commun.* **15**, 211 (2024).

[4] H. Ma, M. Govoni, and G. Galli, Quantum simulations of materials on near-term quantum computers, *npj Comput. Mater.* **6**, 85 (2020).

[5] E. Farhi, J. Goldstone, and S. Gutmann, A quantum approximate optimization algorithm, *arXiv preprint arXiv:1411.4028* (2014).

[6] L. Zhou, S.-T. Wang, S. Choi, H. Pichler, and M. D. Lukin, Quantum approximate optimization algorithm: Performance, mechanism, and implementation on near-term devices, *Phys. Rev. X* **10**, 021067 (2020).

[7] Z. Wang, S. Hadfield, Z. Jiang, and E. G. Rieffel, Quantum approximate optimization algorithm for maxcut: A fermionic view, *Phys. Rev. A* **97**, 022304 (2018).

[8] K. Goswami, P. Schmelcher, and R. Mukherjee, Qudit-based scalable quantum algorithm for solving the integer programming problem, *arXiv preprint arXiv:2508.13906* (2025).

[9] F. Koch, S. Panahiyan, R. Mukherjee, J. Doetsch, and D. Jaksch, Resource-efficient quantum optimization via higher-order encoding, *arXiv preprint arXiv:2511.17545* (2025).

[10] W. Li, Z. Yin, X. Li, D. Ma, S. Yi, Z. Zhang, C. Zou, K. Bu, M. Dai, J. Yue, *et al.*, A hybrid quantum computing pipeline for real world drug discovery, *Sci. Rep.* **14**, 16942 (2024).

[11] N. S. Blunt, J. Camps, O. Crawford, R. Izsák, S. Leonida, A. Mirani, A. E. Moylett, S. A. Scivier, C. Sunderhauf, P. Schopf, *et al.*, Perspective on the current state-of-the-art of quantum computing for drug discovery applications, *J. Chem. Theory Comput.* **18**, 7001 (2022).

[12] A. M. Smaldone, Y. Shee, G. W. Kyro, C. Xu, N. P. Vu, R. Dutta, M. H. Farag, A. Galda, S. Kumar, E. Kyo-seva, *et al.*, Quantum machine learning in drug discovery: Applications in academia and pharmaceutical industries, *Chem. Rev.* **125**, 5436 (2025).

[13] A. Barenco, C. H. Bennett, R. Cleve, D. P. DiVincenzo, N. Margolus, P. Shor, T. Sleator, J. A. Smolin, and H. Weinfurter, Elementary gates for quantum computation, *Phys. Rev. A* **52**, 3457 (1995).

[14] D. P. DiVincenzo, The physical implementation of quantum computation, *Fortschr. Phys.* **48**, 771 (2000).

[15] T. D. Ladd, F. Jelezko, R. Laflamme, Y. Nakamura, C. Monroe, and J. L. O'Brien, Quantum computers, *Nature* **464**, 45 (2010).

[16] A. Montanaro, Quantum algorithms: an overview, *npj Quantum Inf.* **2**, 15023 (2016).

[17] B. M. Terhal, Quantum error correction for quantum memories, *Rev. Mod. Phys.* **87**, 307 (2015).

[18] A. Katabarwa, K. Gratsea, A. Caesura, and P. D. Johnson, Early fault-tolerant quantum computing, *PRX Quantum* **5**, 020101 (2024).

[19] M. Neeley, R. C. Bialczak, M. Lenander, E. Lucero, M. Mariantoni, A. O'connell, D. Sank, H. Wang, M. Weides, J. Wenner, *et al.*, Generation of three-qubit entangled states using superconducting phase qubits, *Nature* **467**, 570 (2010).

[20] F. Arute, K. Arya, R. Babbush, D. Bacon, J. C. Bardin, R. Barends, R. Biswas, S. Boixo, F. G. Brandao, D. A. Buell, *et al.*, Quantum supremacy using a programmable superconducting processor, *Nature* **574**, 505 (2019).

[21] M. Nünnerich, D. Cohen, P. Barthel, P. H. Huber, D. Niroomand, A. Retzker, and C. Wunderlich, Fast, robust, and laser-free universal entangling gates for trapped-ion quantum computing, *Phys. Rev. X* **15**, 021079 (2025).

[22] J. M. Arrazola, V. Bergholm, K. Brádler, T. R. Bromley, M. J. Collins, I. Dhand, A. Fumagalli, T. Gerrits, A. Goussev, L. G. Helt, *et al.*, Quantum circuits with many photons on a programmable nanophotonic chip, *Nature* **591**, 54 (2021).

[23] L. Henriet, L. Beguin, A. Signoles, T. Lahaye, A. Browaeys, G.-O. Reymond, and C. Jurczak, Quantum computing with neutral atoms, *Quantum* **4**, 327 (2020).

[24] H. Zhou, C. Zhao, M. Cain, D. Bluvstein, N. Maskara, C. Duckering, H.-Y. Hu, S.-T. Wang, A. Kubica, and M. D. Lukin, Low-overhead transversal fault tolerance for universal quantum computation, *Nature* **646**, 303 (2025).

[25] K. R. Brown, J. Kim, and C. Monroe, Co-designing a scalable quantum computer with trapped atomic ions, *npj Quantum Inf.* **2**, 1 (2016).

[26] S. Jandura, J. D. Thompson, and G. Pupillo, Optimizing rydberg gates for logical-qubit performance, *PRX Quantum* **4**, 020336 (2023).

[27] N. Glaser, F. Roy, I. Tsitsilin, L. Koch, N. Bruckmoser, J. Schirk, J. Romeiro, G. Huber, F. Wallner, M. Singh, *et al.*, Closed-loop optimization for high-fidelity controlled-z gates in superconducting qubits, *Phys. Rev. Appl.* **24**, 024048 (2025).

[28] E. Y. Egorova, A. S. Kazmina, I. A. Simakov, I. N. Moskalenko, N. N. Abramov, D. A. Kalacheva, V. B. Lubsanov, A. N. Bolgar, N. Maleeva, and I. S. Besedin, Three-mode tunable coupler for superconducting two-qubit gates, *Phys. Rev. Appl.* **23**, 064056 (2025).

[29] W.-J. Lin, H. Cho, Y. Chen, M. G. Vavilov, C. Wang, and V. E. Manucharyan, 24 days-stable cnot gate on fluxonium qubits with over 99.9% fidelity, *PRX Quantum* **6**, 010349 (2025).

[30] Y. Ye, S. Cao, Y. Wu, X. Chen, Q. Zhu, S. Li, F. Chen, M. Gong, C. Zha, H.-L. Huang, *et al.*, Realization of high-fidelity controlled-phase gates in extensible superconducting qubits design with a tunable coupler, *Chin. Phys. Lett.* **38**, 100301 (2021).

[31] R. Barends, J. Kelly, A. Megrant, A. Veitia, D. Sank, E. Jeffrey, T. C. White, J. Mutus, A. G. Fowler, B. Campbell, *et al.*, Superconducting quantum circuits at the surface code threshold for fault tolerance, *Nature* **508**, 500 (2014).

[32] A. Kandala, K. Temme, A. D. Córcoles, A. Mezzacapo, J. M. Chow, and J. M. Gambetta, Error mitigation extends the computational reach of a noisy quantum processor, *Nature* **567**, 491 (2019).

[33] E. Knill, R. Laflamme, and G. J. Milburn, A scheme for efficient quantum computation with linear optics, *Nature* **409**, 46 (2001).

[34] P. Kok, W. J. Munro, K. Nemoto, T. C. Ralph, J. P. Dowling, and G. J. Milburn, Linear optical quantum computing with photonic qubits, *Rev. Mod. Phys.* **79**, 135 (2007).

[35] M. Saffman, T. G. Walker, and K. Mølmer, Quantum information with rydberg atoms, *Rev. Mod. Phys.* **82**, 2313 (2010).

[36] H. Levine, A. Keesling, G. Semeghini, A. Omran, T. T. Wang, S. Ebadi, H. Bernien, M. Greiner, V. Vuletić, H. Pichler, and M. D. Lukin, Parallel implementation of high-fidelity multi-qubit gates with neutral atoms, *Phys. Rev. Lett.* **123**, 170503 (2019).

[37] T. M. Graham, M. Kwon, B. Grinkemeyer, Z. Marra, X. Jiang, M. T. Lichtman, Y. Sun, M. Ebert, and M. Saffman, Rydberg-mediated entanglement in a two-dimensional neutral atom qubit array, *Phys. Rev. Lett.* **123**, 230501 (2019).

[38] D. Bluvstein, H. Levine, G. Semeghini, T. T. Wang, S. Ebadi, M. Kalinowski, A. Keesling, N. Maskara, H. Pichler, M. Greiner, V. Vuletić, and M. D. Lukin, A quantum processor based on coherent transport of entangled atom arrays, *Nature* **604**, 451 (2022).

[39] D. Bluvstein, S. J. Evered, A. A. Geim, S. H. Li, H. Zhou, T. Manovitz, S. Ebadi, M. Cain, M. Kalinowski, J. P. B. Ataides, N. Maskara, I. Cong, X. Gao, M. Greiner, V. Vuletić, and M. D. Lukin, Logical quantum processor based on reconfigurable atom arrays, *Nature* **626**, 58 (2024).

[40] S. J. Evered, D. Bluvstein, M. Kalinowski, S. Ebadi, T. Manovitz, H. Zhou, S. H. Li, A. A. Geim, ..., and M. D. Lukin, High-fidelity parallel entangling gates on a neutral-atom quantum computer, *Nature* (2023), reported scalable, reconfigurable neutral-atom gates.

[41] M. Endres, H. Bernien, A. Keesling, H. Levine, E. R. Anschuetz, A. Krajenbrink, C. Senko, V. Vuletic, M. Greiner, and M. D. Lukin, Atom-by-atom assembly of defect-free one-dimensional cold atom arrays, *Science* **354**, 1024 (2016).

[42] E. Knill, Quantum computing with realistically noisy devices, *Nature* **434**, 39 (2005).

[43] D. Petrosyan, F. Motzoi, M. Saffman, and K. Mølmer, High-fidelity rydberg quantum gate via a two-atom dark state, *Phys. Rev. A* **96**, 042306 (2017).

[44] S. Jandura and G. Pupillo, Time-optimal two-and three-qubit gates for rydberg atoms, *Quantum* **6**, 712 (2022).

[45] D. Jaksch, J. I. Cirac, P. Zoller, S. L. Rolston, R. Côté, and M. D. Lukin, Fast quantum gates for neutral atoms, *Phys. Rev. Lett.* **85**, 2208 (2000).

[46] M. D. Lukin, M. Fleischhauer, R. Cote, L. Duan, D. Jaksch, J. I. Cirac, and P. Zoller, Dipole blockade and quantum information processing in mesoscopic atomic ensembles, *Phys. Rev. Lett.* **87**, 037901 (2001).

[47] X.-F. Shi, Quantum logic and entanglement by neutral rydberg atoms: methods and fidelity, *Quantum Sci. Technol.* **7**, 023002 (2022).

[48] S. Ma, G. Liu, P. Peng, B. Zhang, S. Jandura, J. Claes, A. P. Burgers, G. Pupillo, S. Puri, and J. D. Thompson, High-fidelity gates and mid-circuit erasure conversion in an atomic qubit, *Nature* **622**, 279 (2023).

[49] G. Giudici, S. Veroni, G. Giudice, H. Pichler, and J. Zeiher, Fast entangling gates for rydberg atoms via resonant dipole-dipole interaction, *PRX Quantum* **6**, 030308 (2025).

[50] X. Jiang, J. Scott, M. Friesen, and M. Saffman, Sensitivity of quantum gate fidelity to laser phase and intensity noise, *Phys. Rev. A* **107**, 042611 (2023).

[51] A. Pagano, S. Weber, D. Jaschke, T. Pfau, F. Meinert, S. Montangero, and H. P. Büchler, Error budgeting for a controlled-phase gate with strontium-88 rydberg atoms, *Phys. Rev. Res.* **4**, 033019 (2022).

[52] L. Theis, F. Motzoi, F. Wilhelm, and M. Saffman, High-fidelity rydberg-blockade entangling gate using shaped, analytic pulses, *Phys. Rev. A* **94**, 032306 (2016).

[53] T. Chang, T. Wang, H.-H. Jen, and Y.-C. Chen, High-fidelity rydberg controlled-z gates with optimized pulses, *New J. Phys.* **25**, 123007 (2023).

[54] X.-F. Shi, Accurate quantum logic gates by spin echo in rydberg atoms, *Phys. Rev. Appl.* **10**, 034006 (2018).

[55] S.-L. Su, L.-N. Sun, B.-J. Liu, L.-L. Yan, M.-H. Yung, W. Li, and M. Feng, Rabi-and blockade-error-resilient all-geometric rydberg quantum gates, *Phys. Rev. Appl.* **19**, 044007 (2023).

[56] M. Khazali and K. Mølmer, Controlled-swap gates by tuning of interfering transition pathways in neutral atom arrays, *arXiv preprint arXiv:2511.22214* (2025).

[57] Z.-y. Jin and J. Jing, Geometric quantum gates via dark paths in rydberg atoms, *Phys. Rev. A* **109**, 012619 (2024).

[58] C. Sun, X. Chen, W. Mu, G. Wang, J. You, and X. Shao, Holonomic swap and controlled-swap gates of neutral atoms via selective rydberg pumping, *EPJ Quantum Technol.* **11**, 1 (2024).

[59] F. Jin, J. Geng, and H. Zhou, Nonadiabatic holonomic quantum gates in a decoherence-insensitive space, *Phys. Rev. A* **111**, 022620 (2025).

[60] X. Tan, J.-L. Wu, C. Deng, W.-J. Mao, H.-T. Wang, and X. Ji, Implementation of quantum phase gate between two atoms via rydberg antiblockade and adiabatic passage, *Chin. Phys. B* **27**, 100307 (2018).

[61] J. Cui, R. Van Bijnen, T. Pohl, S. Montangero, and T. Calarco, Optimal control of rydberg lattice gases, *Quantum Sci. Technol.* **2**, 035006 (2017).

[62] R. Mukherjee, F. Sauvage, H. Xie, R. Löw, and F. Mintert, Preparation of ordered states in ultra-cold gases using bayesian optimization, *New J. Phys.* **22**, 075001 (2020).

[63] R. Mukherjee, H. Xie, and F. Mintert, Bayesian optimal control of greenberger-horne-zeilinger states in rydberg lattices, *Phys. Rev. Lett.* **125**, 203603 (2020).

[64] G. Doulsinos, A. Delakouras, and D. Petrosyan, Fundamental bound on entanglement generation between interacting rydberg atoms, *arXiv preprint arXiv:2512.13379* (2025).

[65] See the Supplemental Material for the derivation of the effective Hamiltonian, the phase noise analysis, model parameters and the Rydberg decay, and the exact solution of the resonant dark state gate.

[66] S. Weber, C. Tresp, H. Menke, A. Urvoy, O. Firstenberg, H. P. Büchler, and S. Hofferberth, Calculation of rydberg interaction potentials, *J. Phys. B: At. Mol. Opt. Phys.* **50**, 133001 (2017).

[67] S. J. Evered, D. Bluvstein, M. Kalinowski, S. Ebadi, T. Manovitz, H. Zhou, S. H. Li, A. A. Geim, T. T. Wang, N. Maskara, *et al.*, High-fidelity parallel entangling gates on a neutral-atom quantum computer, *Nature* **622**, 268 (2023).

[68] R. B.-S. Tsai, X. Sun, A. L. Shaw, R. Finkelstein, and M. Endres, Benchmarking and fidelity response theory of high-fidelity rydberg entangling gates, *PRX Quantum* **6**, 010331 (2025).

[69] Z. Zhang, M. Yuan, B. Sundar, and K. R. Hazzard, Motional decoherence in ultracold-rydberg-atom quantum simulators of spin models, *Phys. Rev. A* **110**, 053321 (2024).

- [70] C. Ates, T. Pohl, T. Pattard, and J. M. Rost, Many-body theory of excitation dynamics in an ultracold rydberg gas, *Phys. Rev. A* **76**, 013413 (2007).
- [71] M. Magoni, R. Joshi, and I. Lesanovsky, Molecular dynamics in rydberg tweezer arrays: Spin-phonon entanglement and jahn-teller effect, *Phys. Rev. Lett.* **131**, 093002 (2023).
- [72] P. P. Mazza, R. Schmidt, and I. Lesanovsky, Vibrational dressing in kinetically constrained rydberg spin systems, *Phys. Rev. Lett.* **125**, 033602 (2020).
- [73] F. M. Gambetta, W. Li, F. Schmidt-Kaler, and I. Lesanovsky, Engineering nonbinary rydberg interactions via phonons in an optical lattice, *Phys. Rev. Lett.* **124**, 043402 (2020).
- [74] A. Parvej and L. Mathey, Lamb-dicke dynamics of interacting rydberg atoms coupled to the motion of an optical tweezer array, *arXiv preprint arXiv:2506.22669* (2025).
- [75] C. Fromonteil, D. Bluvstein, and H. Pichler, Protocols for rydberg entangling gates featuring robustness against quasistatic errors, *PRX Quantum* **4**, 020335 (2023).
- [76] S. de Léséleuc, D. Barredo, V. Lienhard, A. Browaeys, and T. Lahaye, Analysis of imperfections in the coherent optical excitation of single atoms to rydberg states, *Phys. Rev. A* **97**, 053803 (2018).

SUPPLEMENTAL MATERIAL
“HIGH-FIDELITY NON-ADIABATIC DARK STATE GATES FOR NEUTRAL ATOMS”

Nader Mostaan¹, Kapil Goswami², Peter Schmelcher^{1,2}, Rick Mukherjee^{1,3,4}

¹*Zentrum für Optische Quantentechnologien, Universität Hamburg, Luruper Chaussee 149, 22761 Hamburg, Germany*

²*The Hamburg Centre for Ultrafast Imaging, Universität Hamburg, Luruper Chaussee 149, 22761 Hamburg, Germany*

³*Department of Physics & Astronomy, University of Tennessee, Chattanooga, TN 37403, USA*

⁴*UTC Quantum Center, University of Tennessee, Chattanooga, TN 37403, USA*

DERIVATION OF THE EFFECTIVE HAMILTONIAN

In Schrieffer-Wolf transformation, an effective Hamiltonian for the relevant states in the target subspace is obtained by eliminating the coupling of these states to the high energy subspace of the Hilbert space to second order in terms of the coupling strength relative to the energy difference to the high energy subspace. If the initial Hamiltonian is expressed as $\hat{H} = \hat{H}_0 + \hat{H}_{\text{pert}}$ where \hat{H}_{pert} is a perturbation to \hat{H}_0 , the Schrieffer-Wolf transformation is carried out by finding the anti-hermitian operator \hat{S} which eliminates \hat{H}_{pert} to the second order as the following,

$$\begin{aligned} e^{-\hat{S}} \hat{H} e^{\hat{S}} &= \hat{H}_0 + \sum_{N=0}^{\infty} \left(\frac{(-1)^N}{N!} + \frac{(-1)^{N+1}}{(N+1)!} \right) \text{Ad}_{\hat{S}}(\hat{H}_{\text{pert}}) \\ &= \hat{H}_0 - \frac{1}{2} [\hat{S}, \hat{H}_{\text{pert}}] + \frac{1}{3} [\hat{S}, [\hat{S}, \hat{H}_{\text{pert}}]] + \dots, \end{aligned} \quad (\text{S1})$$

where $\text{Ad}_{\hat{S}}(\hat{H}_{\text{pert}}) = [\hat{S}, \hat{H}_{\text{pert}}]$. Equation S1 is obtained by requiring that $[\hat{S}, \hat{H}_0] = \hat{V}$. The unperturbed Hamiltonian can be cast into a block diagonal form

$$\hat{H}_0 = \begin{bmatrix} \hat{H}_L & 0 \\ 0 & \hat{H}_H \end{bmatrix} \quad (\text{S2})$$

and the perturbation \hat{V} takes the form

$$\hat{H}_{\text{pert}} = \begin{bmatrix} 0 & \hat{V} \\ \hat{V} & 0 \end{bmatrix}, \quad (\text{S3})$$

in this case, it is sufficient to choose \hat{S} by the form

$$\hat{S} = -i \begin{bmatrix} 0 & \hat{T} \\ \hat{T}^\dagger & 0 \end{bmatrix}, \quad (\text{S4})$$

Here, \hat{T} can be solved to yield $\hat{T} = i\hat{V}\hat{H}_H^{-1}$. Thus, the effective Hamiltonian in the low energy subspace reads

$$\hat{H}_{\text{eff}} = \hat{H}_L - \hat{V}\hat{H}_H^{-1}\hat{V}^\dagger + \mathcal{O}(\hat{V}^3), \quad (\text{S5})$$

PHASE NOISE ANALYSIS

Here we follow Ref. [76] and [50] to carry out phase noise analysis of the adiabatic and non-adiabatic dark state gates as well as the time optimal blockade gate. We start with the power spectral density of the detuning noise noise defined by

$$S_\nu(f) = \frac{a_\nu}{f} + \frac{hf_{\text{cav}}(\delta f_{\text{cav}})^2}{\bar{P}} \left[1 + \alpha^2 \frac{f_{rlx}^4}{(f_{rlx}^2 - f^2)^2 - 4\gamma f_{rlx}^2 f^2} \right]. \quad (\text{S6})$$

where a_ν is the low-frequency white noise level, $f_{\text{cav}} = c/\lambda_L$ the laser frequency, δf_{cav} is the FWHM laser cavity linewidth, \bar{P} is the time-averaged laser power, α is the linewidth enhancement factor, f_{rlx} is the relaxation frequency

of the semiconductor laser carriers and γ the damping factor. By filtering the phase noise through a cavity, the filtered phase noise takes the following form

$$S_{\nu,\text{out}}(f) = |H_L(if)|^2 [S_{\nu,\text{in}}(f) - S_{\nu,\text{QNL}}(f)] + S_{\nu,\text{QNL}}(f), \quad (\text{S7})$$

where $H_L(s)$ is the frequency response function of the filter, given by

$$H_L(s) = \sqrt{a_s} + (1 - \sqrt{a_s})H_{\text{HP},1}(s) \left(1 + (\sqrt{a_p} - 1)H_{\text{BP}}(s) \right), \quad (\text{S8})$$

with $H_{\text{HP},1}(s) = s/(s + f_c)$, $H_{\text{BP}}(s) = 2\gamma_p f_p s / (s^2 + 2\gamma_p f_p s + f_p^2)$ and $f_p = f_c(1 + 2\gamma_p)\sqrt{a_p}$. The filter parameters as well as the noise parameters are given in Table. S1.

a_ν (MHz)	λ_L (nm)	δf_{cav} (GHz)	P (mW)	α	f_{rlx} (GHz)	γ	a_s	a_p	f_c (MHz)	γ_p
10	302	4	500	5	10	0.125	0.1	2	1	1

TABLE S1. Decay rates of the Rydberg states involved in the gate dynamics.

The phase noise power spectral density is then obtained from $S_{\nu,\text{out}}(f)$ in Eq. S7 by $S_\phi(f) = S_{\nu,\text{out}}(f)/f^2$, and the single-side-band (SSB) form of $S_\phi(f)$ is obtained according to $S_{\text{SSB}}^\phi(f) = 2S_\phi(f)$ for $f > 0$. To construct phase noise samples we use the formula

$$\sigma_\phi(f_k) = \sqrt{\frac{T_{\text{meas}}}{2\Delta t^2} S_{\text{SSB}}^\phi(f)}, \quad (\text{S9})$$

where $T_{\text{meas}} = 5\text{ ms}$ is the total measurement time of the phase noise, $\Delta t = T_{\text{meas}}/(2N_s + 1)$ with $N_s = 5 \times 10^6$ the number of noise sample bins, $\sigma_\phi^2(f_k)$ is the variance of a normally distributed random variable representing the magnitude of the phase noise at frequency $f_k = k/T_{\text{meas}}$, $k = 1, \dots, N_s$. The time domain random samples of the phase noise are obtained by taking the discrete Fourier transform of the frequency domain samples generated according to this normal distribution for the amplitude, and a uniform distribution for the phase of the samples.

A. Rydberg decay

The decay rates obtained by the `PairInteraction` package for the different Rydberg states including the black-body radiation at the temperature $T_{\text{th}} = 1\text{ }\mu\text{K}$ are tabulated in Table. S2.

n	$\Gamma_{nP_{3/2}}$ (kHz)	$\Gamma_{nS_{1/2}}$ (kHz)	$\Gamma_{(n+1)S_{1/2}}$ (kHz)
40	6.88	17.53	16.14
50	3.20	8.30	7.77
60	1.74	4.57	4.33
70	1.06	2.78	2.66

TABLE S2. Decay rates of the Rydberg states involved in the gate dynamics.

B. Exact solution of the dark state gate

the eigenstates and eigenvalues of $\hat{H}_{11,\text{DarkState}}(t)$ can be obtained exactly. Defining $\mathcal{B} = (B^4 + \Omega_C^2 \Omega_T^2)^{1/4}$, the eigenenergies are $\{\epsilon_0 = 0, \pm\epsilon_-, \pm\epsilon_+\}$, where $\epsilon_\pm = (1/2)\sqrt{(2B^2 + \Omega_C^2 + \Omega_T^2) \pm 2\mathcal{B}^2}$. The normalized states are

$$\left\{ \begin{array}{l} |\epsilon_0\rangle = \frac{1}{N_0} \left[0, -e^{-i\varphi_C} \Omega_C, e^{-i\varphi_T} \Omega_T, 0, \frac{\Omega_C^2 - \Omega_T^2}{2B} \right]^T, \\ |-\epsilon_-\rangle = \frac{1}{N_-} \left[\frac{\epsilon_-(B^2 + \mathcal{B}^2)}{B\Omega_C\Omega_T}, -\frac{e^{-i\varphi_C}(B^2 + \mathcal{B}^2 - \Omega_C^2)}{2B\Omega_C}, -\frac{e^{-i\varphi_T}(B^2 + \mathcal{B}^2 - \Omega_T^2)}{2B\Omega_T}, -\frac{\epsilon_-}{B}, 1 \right]^T, \\ |+\epsilon_-\rangle = \frac{1}{N_-} \left[-\frac{\epsilon_-(B^2 + \mathcal{B}^2)}{B\Omega_C\Omega_T}, -\frac{e^{-i\varphi_C}(B^2 + \mathcal{B}^2 - \Omega_C^2)}{2B\Omega_C}, -\frac{e^{-i\varphi_T}(B^2 + \mathcal{B}^2 - \Omega_T^2)}{2B\Omega_T}, \frac{\epsilon_-}{B}, 1 \right]^T, \\ |-\epsilon_+\rangle = \frac{1}{N_+} \left[\frac{\epsilon_+(B^2 - \mathcal{B}^2)}{B\Omega_C\Omega_T}, -\frac{e^{-i\varphi_C}(B^2 - \mathcal{B}^2 - \Omega_C^2)}{2B\Omega_C}, -\frac{e^{-i\varphi_T}(B^2 - \mathcal{B}^2 - \Omega_T^2)}{2B\Omega_T}, -\frac{\epsilon_+}{B}, 1 \right]^T, \\ |+\epsilon_+\rangle = \frac{1}{N_+} \left[-\frac{\epsilon_+(B^2 - \mathcal{B}^2)}{B\Omega_C\Omega_T}, -\frac{e^{-i\varphi_C}(B^2 - \mathcal{B}^2 - \Omega_C^2)}{2B\Omega_C}, -\frac{e^{-i\varphi_T}(B^2 - \mathcal{B}^2 - \Omega_T^2)}{2B\Omega_T}, \frac{\epsilon_+}{B}, 1 \right]^T, \end{array} \right. \quad (\text{S10})$$

with norms

$$\begin{cases} \mathcal{N}_0 = \sqrt{(\Omega_C^2 + \Omega_T^2) + \frac{(\Omega_C^2 - \Omega_T^2)^2}{4B^2}}, \\ \mathcal{N}_{\pm} = \sqrt{\frac{(\Omega_C^2 + \Omega_T^2)(B^2 \mp \mathcal{B}^2)}{\Omega_C^2 \Omega_T^2} + \frac{(\Omega_C^2 + \Omega_T^2) \pm 2\mathcal{B}^2}{B^2}}. \end{cases} \quad (\text{S11})$$

The limit of $\Omega_C, \Omega_T \ll B$ is of particular interest. In this limit, a straightforward Taylor expansion in Ω_C/B and Ω_T/B shows that the leading order contribution of finite B in $\hat{H}_{11, \text{DarkState}}(t)$ comes at the second order in $\Omega_{C(T)}/B$.

When $\Omega_C = 0, \Omega_T \neq 0$ or $\Omega_T = 0, \Omega_C \neq 0$, the level scheme reduces to the one for the dark state gate. In this case, $|\pm\epsilon_-\rangle$ represent the single-Rydberg-excitation states that are coupled via the nonzero Rabi pulse, $|\epsilon_0\rangle$ reduces to the dark state, and $|\pm\epsilon_+\rangle$ represent far off-resonant states.